

Title: HP-PbF₂-type FeCl₂ as a potential Cl-carrier in the deep Earth

Manuscript Number: 8283R

Authors: Hongsheng Yuan, Center for High Pressure Science and Technology Advanced Research Lianjie Man, Center for High Pressure Science and Technology Advanced Research Duck Young Kim, Center for High Pressure Science and Technology Advanced Research Dmitry Popov, Argonne National Laboratory Yue Meng, Argonne National Laboratory Eran Greenberg, Tel Aviv University Vitali Prakapenka, Consortium for Advanced Radiation Source (CARS) Li Zhang, Center for High Pressure Science and Technology Advanced Research

1 **HP-PbF₂-type FeCl₂ as a potential Cl-carrier in the deep Earth (Revision 1)**

2 *Hongsheng Yuan^{1*}, Lianjie Man¹, Duck Young Kim¹, Dmitry Popov², Yue Meng², Eran*
3 *Greenberg^{3¶}, Vitali Prakapenka³, and Li Zhang^{1*}*

4 ¹Center for High Pressure Science and Technology Advanced Research (HPSTAR), Shanghai
5 201203, China

6 ²HPCAT, X-ray Science Division, Argonne National Laboratory, Argonne, IL 60439, U.S.A.

7 ³GeoSoilEnviroCARS, University of Chicago, Chicago, Illinois 60637, USA.

8

9

10 *Corresponding author: Hongsheng Yuan(hongsheng.yuan@hpstar.ac.cn), Li Zhang
11 (zhangli@hpstar.ac.cn)

12 ¶ Present address: Eran Greenberg: Applied Physics Division, Soreq Nuclear Research Center
13 (SNRC), Yavne 81800, Israel.

14

15

16 **Abstract**

17 We report for the first time the formation of a HP-PbF₂-type FeCl₂ phase (space group: $Pa\bar{3}$),
18 through high pressure-temperature (P - T) reactions in the hydrous systems (Mg_{0.6}Fe_{0.4})SiO₃-
19 H₂O-NaCl and FeO₂H-NaCl in a laser-heated diamond anvil cell up to 108 GPa and 2000 K.
20 Applying single-crystal X-ray diffraction (XRD) analysis to individual submicron-sized grains,
21 we have successfully determined the **crystal** structure of the as-synthesized FeCl₂ phase, in
22 agreement with our theoretical structure search results. In-situ high P - T XRD data revealed the
23 substitution of Cl for OH(O) in such a cubic $Pa\bar{3}$ symmetry, demonstrating that this topology is
24 a potential host for both H and Cl in the deep Earth. The chemical analysis on the recovered
25 sample showed a considerable Na₂O content and an abundance of ferric iron in the post-
26 perovskite phase. The coexistence of the cubic FeCl₂ **phase** and post-perovskite suggests that the
27 lowermost mantle could be a potential reservoir of Cl. The possible presence of volatiles such as
28 H and Cl in the deep lower mantle would impact the composition and iron valence state of the
29 post-perovskite phase.

30

31 Keywords: iron chloride, multigrain X-ray diffraction, lower mantle, hydrogen and chlorine
32 cycle, post-pervoskite

33

34 **Introduction**

35 Cl is abundant in seawater and most geological fluids. Owing to its hydrophilic behavior,
36 Cl abundances and isotopic data provide important information on geological processes
37 (Bonifacie et al. 2008; Sharp et al. 2010). Hydrous minerals have been shown to be major Cl
38 carriers from oceanic to deep subduction environments (Kendrick et al. 2017). Serpentinites act
39 as the major carriers of H (or H₂O) and Cl, and subducting serpentinites play an important role in
40 the recycling of Cl (Scambelluri and Philippot 2001). Mass balance calculations suggest that Cl
41 inputs exceed outputs at certain subduction zones (Barnes and Straub 2010; John et al. 2011).
42 This is consistent with the observations of Mg-, Fe- and alkali-rich saline fluids containing up to
43 50 wt% Cl, Na, K, Mg and Fe trapped as inclusions inside high-pressure vein minerals in many
44 eclogitic terranes, suggesting that Cl is recycling back into the mantle by subduction
45 (Scambelluri et al. 1997).

46 There is a growing body of research that focuses on the storage potential of halogens and
47 hydrogen in the mantle. Roberge et al. (2017) showed that the Cl contents in hydrous wadsleyite
48 and ringwoodite ranging from 60 ±60 to 200 ±48 ppm are much lower than their F contents that
49 range from 186 ±19 to 850 ±85 ppm, but that the substitution correlations of Cl⁻ with OH⁻
50 remain unclear. Yoshino & Jaseem (2018) found that incorporation of water and alumina greatly
51 enhances F solubility in bridgmanite, exceeding 1 wt%, showing a sufficient capacity to store the
52 whole F budget. The ionic radius of Cl⁻ is significantly larger than that of F⁻, so that the Cl
53 solubility in the mantle silicates is expected to be very low. The major host for Cl in the deep
54 mantle remains unknown. Du et al. (2018) predict a series of stable structures of iron chlorides
55 including Fe₃Cl, Fe₂Cl, FeCl, FeCl₂, FeCl₃ and FeCl₄ in the pressure range of Earth's mantle and
56 core.

57 Recent studies showed that the pyrite-structured FeO_2 and FeO_2H_x ($x \leq 1$) phase was
58 observed under P - T conditions representative of the deep lower mantle (DLM) (Hu et al. 2016;
59 Liu et al. 2017; Mao et al. 2017; Nishi et al. 2017; Yuan et al. 2018). The latest study by E.
60 Koemets et al. (2021) argued that FeO_2 and FeO_2H_x adopt HP-PdF₂-type other than pyrite-type
61 structure due to the absence of the O–O covalent bonds. In spite of the controversy, we termed
62 this cubic FeO_2H_x as “py-phase” in this work. As an important hydrogen carrier, the py-phase
63 has been experimentally confirmed to be stable in the DLM along average mantle geotherm.
64 Koemets et al. (2020) reported a novel $\text{Na}_2\text{FeCl}_4\text{OH}_x$ phase through chemical reactions between
65 FeO_2H and NaCl under high P - T conditions. It is intriguing to explore the potential relation of
66 hydrogen and chlorine in the Fe-bearing system in the DLM. Here we report the first
67 experimental discovery of a cubic FeCl_2 phase, referred to as “c- FeCl_2 ”, coexisting with a post-
68 perovskite (pPv) phase in the system $(\text{Mg,Fe})\text{SiO}_3$ – H_2O – NaCl . We demonstrated replacement of
69 OH(O) by Cl in the cubic $Pa\bar{3}$ structure, providing a new hydrogen-chlorine relation under the
70 P - T conditions of the DLM.

71 **Methods**

72 We used goethite (α - FeO_2H) powder (99+% purity, Alfa Aesar) and synthesized
73 $\text{Mg}_{0.6}\text{Fe}_{0.4}\text{SiO}_3$ orthopyroxene (En60) as the starting samples. Three hydrous sample assemblies
74 $(\text{Mg}_{0.6}\text{Fe}_{0.4})\text{SiO}_3(\text{En60})$ – NaCl – H_2O (Run CHS06), En60 – H_2O (Run CSb003) and α - FeO_2H –
75 NaCl (Run ETR3) were designed for this study. In-situ synchrotron XRD experiments were
76 performed at HPCAT (Sector 16) (Meng et al. 2015) and GeoSoilEnviroCARS (the University of
77 Chicago, Sector 13) (Prakapenka et al. 2008), Advanced Photon Source (APS), Argonne
78 National Laboratory. Decompression XRD experiments were performed at beamline 15U1,
79 Shanghai Synchrotron Radiation Facility (SSRF), China. The starting assemblies, P - T conditions

80 and heating duration are summarized in Table S1 in the supporting information. Complementary
81 to the in-situ XRD characterization, ex-situ chemical analysis was performed on the recovered
82 sample of Run CHS06 by a transmission electron microscope (TEM) coupled with an energy
83 dispersive X-ray spectroscopy (EDS). We also conducted first-principles calculations to examine
84 the stability, structure and electronic properties of FeCl₂ from the Fe–Cl system. See supporting
85 information for details of methods.

86 **Results and discussion**

87 The sample assembly En60–NaCl–H₂O was compressed to 108(2) GPa at room *T* and
88 heated at 1950(200) K, and we observed the appearance of the pPv phase along with several
89 additional sharp peaks while the diffraction lines of NaCl vanished following heating (Fig. 1a
90 and Fig. S1 in the supporting information), indicating a chemical reaction occurring in this
91 system. For comparison, previous experiments on dry (Mg,Fe)SiO₃ orthopyroxene using NaCl
92 medium under similar *P-T* conditions did not show any sign of reaction (e.g. Dorfman et al.,
93 2013). To investigate the role of water in this reaction, we further conducted high *P-T*
94 experiments on an assemblage of En60–H₂O without NaCl. As shown in Figure 1b, the
95 diffraction peaks can be well indexed by the coexistence of the pPv and py-phase at 115(2) GPa
96 after 2150(200) K heating, indicating a reaction between En60 and water. The py-phase has a
97 lattice parameter of $a = 4.3676(2) \text{ \AA}$ at 115 GPa and after *T* quench. Notably, the new peaks
98 (marked by “C”) observed in the system En60–NaCl–H₂O can be well indexed by a cubic lattice
99 with $a = 4.9490(2) \text{ \AA}$ at 108(2) GPa (Fig. 1a). The combined results suggest that the py-phase
100 might react with NaCl under similar *P-T* conditions.

101 To examine the formation mechanism of the new cubic phase, we performed high P - T
102 experiments on the assemblage of α -FeO₂H–NaCl. The sample was first compressed to around
103 100 GPa at room temperature. As shown in Fig. 2a, sharp peaks of the py-phase were observed
104 within the first two minutes of heating at 1700(200) K. Increasing T to 2000(200) K and heating
105 the sample for another two minutes, we observed the appearance of new peaks together with
106 formation of crystalline ice X (Loubeyre et al. 1999) at the expense of the py-phase. The
107 dominant new phase(s) were preserved after T quench together with small amounts of the
108 residual py-phase (Fig. 2b). The residual py-phase was indexed with $a= 4.4079(8)$ Å at 100(2)
109 GPa, which is consistent with the values measured by previous studies (Nishi et al. 2017, Hu et
110 al. 2016). Similar to the cubic phase found in the system En60–NaCl–H₂O at 108(2) GPa, a
111 significant portion of the new peaks can be indexed by a cubic lattice with $a= 4.9779(6)$ Å at
112 100(2) GPa (Fig. 2b). The remaining diffractions cannot be indexed straightforwardly. We
113 carried out another high P - T XRD (Run CSa010) at 96(2) GPa, and the sample was heated at
114 2050(200) K for 10 minutes (Fig. 2c). No py-phase can be observed in this run and the
115 diffraction (110) of NaCl-B2 phase is strong in intensity, suggesting that the long-time heating
116 duration and/or a larger ratio of NaCl:FeO₂H at the interface leads to a complete reaction. As
117 seen in Fig. 2c, except for ice X, NaCl and the new cubic phase with $a= 4.9822(2)$ Å, there were
118 strong unidentified diffractions at lower diffraction angle, and similar diffractions with less
119 pronounced intensity were observed in Run ETR3 (Fig. 2b).

120 During the preparation of this paper, it has come to our attention that the interaction
121 between FeO₂H and NaCl was explored by Koemets et al. (2020). Indeed, **identification of the**
122 **products is a complex issue.** They **identified** the products **as a mixture of** two orthorhombic
123 phases. And one of **the phases** was determined with a chemical formula of Na₂FeCl₄OH _{x} by

124 single-crystal XRD analysis at 107(2) GPa after 2400(200) K heating. As shown in Fig. 2c, we
125 found that the calculated diffraction positions of the $\text{Na}_2\text{FeCl}_4\text{OH}_x$ phase together with the new
126 cubic phase could well match most of the diffractions of the products in our experiment Run
127 CSa010. On the other hand, the other orthorhombic phase they proposed (denoted as “oI phase”)
128 was not present in the run products of our experiment. The applied lower T of 2000 K may result
129 in the absence of the oI phase and the presence of a new cubic phase in the current study,
130 whereas the opposite situation occurred by heating at a higher T of 2400 K in the study of
131 Koemets et al (2020). The structure solutions for all the products in the system $\text{FeO}_2\text{H-NaCl}$
132 should be further investigated but beyond the scope of this work.

133 Importantly, the new cubic phase with $a=4.95\text{--}4.98\text{ \AA}$ is repeatably produced in the
134 systems $\text{En60-NaCl-H}_2\text{O}$ and $\text{FeO}_2\text{H-NaCl}$ at pressures of 96–108 GPa. We applied the
135 multigrain XRD technique to index individual grains of the new cubic phase, following the
136 procedures described in a previous study (Zhang et al. 2019). The crystal structure of the cubic
137 phase was determined without prior knowledge of its chemical composition. Only two atomic
138 positions are required to be filled in the structure and we obtained a reasonable structure model
139 by filling the positions with Fe and Cl, respectively, indicating the HP- PbF_2 -type FeCl_2 (see
140 supporting information for details of single-crystal refinements).

141 Our theoretical prediction at 100 GPa shows FeCl_2 and FeCl_3 are energetically stable,
142 while FeCl_4 becomes close to the convex hull line (Fig. 3a). The calculated structure of the FeCl_2
143 phase is in agreement with the experimental results (Table S2 in the supporting information).
144 With a DFT+U approach, the cubic FeCl_2 is calculated to be an indirect band gap semiconductor
145 with 0.1 eV (Fig. 3b. See supporting information for electronic properties of HP- PdF_2 -type
146 FeCl_2). Stable phonon dispersion curves of FeCl_2 at 30 and 100 GPa in our calculations suggest

147 the stability of HP-PdF₂-type FeCl₂ in a broad pressure range (Fig. 3c and d). **Indeed, we found**
148 **that the HP-PbF₂-type FeCl₂ phase is stable at ~29 GPa during decompression (Fig. S2 in the**
149 **supporting information).** Since unit-cell parameters of the coexisting py-phase and HP-PdF₂-type
150 FeCl₂ in Run ETR3 are well consistent with the previous experimental and calculated values of
151 the endmembers, respectively, solid solutions between these two phases appear unlikely to be
152 formed.

153 **Geophysical implications**

154 Previous studies showed that both metallic Fe and Fe oxides react with H₂O, producing
155 the py-phase in the DLM. Yuan et al. (2019) demonstrated the coexistence of the py-phase and a
156 pPv phase in a simplified Fe³⁺-bearing hydrous subducted slab composition. We further found
157 that En60 with Fe²⁺ reacts with H₂O, producing the py-phase coexisting with a pPv phase. These
158 combined results suggest that the py-phase can be generally formed by the redox reactions
159 between water and Fe-bearing minerals with Fe in different valence states. With the addition of
160 NaCl, the HP-PdF₂-type FeCl₂ was produced in place of the py-phase through high *P-T* reactions
161 in the systems FeO₂H–NaCl and En60–H₂O–NaCl. In comparison, a chemical reaction between
162 CO₂ and py-phase was observed in the Fe–C–O–H system, producing a tetrahedral carbonate
163 phase Fe₄C₃O₁₂ at the expense of the py-phase above 2300 K (Boulard et al., 2018). Although
164 the iron valence state of py-phase is still under debate, it is clear that the reaction product of
165 Fe₄C₃O₁₂ contains only Fe³⁺ in the carbon-bearing system, while total Fe²⁺ is found for FeCl₂ in
166 the chlorine-bearing system. These investigations suggest that the deep Earth volatile cycles
167 including hydrogen, carbon and chlorine are correlated in a more complex way than previously
168 thought, suggesting a volatile-dependent Fe²⁺/Fe³⁺ ratio heterogeneity in the DLM.

169 The recent discovery of Ice-VII and halite inclusions in the deep mantle diamonds
170 provides direct evidence for the existence of saline fluid in the shallow lower mantle at least
171 regionally (Tschauner et al. 2018). A recent isotopic study showed that Cl-rich melt inclusions
172 are associated with radiogenic Pb isotopes in the lower-mantle sourced olivine samples,
173 indicating that surface Cl in the ancient seawater-altered and carbonated oceanic crust has been
174 conveyed downward to the lower mantle (Hanyu et al. 2019). These geochemical and isotopic
175 studies show that a considerable Cl (i.e 13–26% or an even greater proportion of the total Cl in
176 the mantle) might have been cycled into lower mantle by slab subduction. However, Cl-bearing
177 phases have not been identified so far in subducted oceanic crust beyond sub-arc depth. Our
178 present results reveal that HP-PdF₂-type FeCl₂ phase is stable at depths beyond 30 GPa to the
179 base of the lower mantle. Since Cl is incompatible with major minerals, Cl can possibly survive
180 in mineral grain boundaries in a cold slab (Hiraga et al. 2004). When the Cl component interacts
181 with hydrous Fe-bearing minerals at greater depths, forming HP-PdF₂-type FeCl₂ phase, this
182 phase would potentially deliver Cl into the deep Earth.

183 The Na₂FeCl₄OH_x phase can be observed in the system FeO₂H–NaCl but absent in the
184 system En60–H₂O–NaCl. The Na component may go into the pPv phase. Indeed, our TEM-EDS
185 results showed that the pPv phase in the En60–H₂O–NaCl system contains ~3 wt.% Na₂O
186 (Fig.S3 and Table S3 in the supporting information). Considering the pPv phase with a chemical
187 formula on the join [(Mg,Fe²⁺)_{1-x}(Fe³⁺,Fe³⁺)_{2x}Si_{1-x}O₃]-Na₂SiO₃, the abundance of ferric iron
188 (Fe³⁺/total Fe ratio) is estimated to be ~0.6. Hirose et al. (2005) showed that 5 wt.% Na₂O
189 together with a high Fe³⁺/total Fe ratio up to 0.8 is incorporated in the pPv phase with a Mid
190 Ocean Ridge Basalt starting composition. Therefore, the presence of volatiles such as H and Cl
191 would impact the composition and iron valence state of the pPv phase in the DLM. Furthermore,

192 we found a **possible** partial melt coexisting with pPv and FeCl₂ from the combined high *P-T*
193 XRD and chemical analysis results. Such a volatile-assisted melting process in the DLM may
194 account for the seismic observations such as ultralow velocity zones (Ren et al. 2007) and large
195 low-shear-velocity provinces (Ford et al. 2006).

196 **Acknowledgments**

197 The authors acknowledge the support from the National Natural Science Foundation of China
198 (NSFC) (Grant No: 41902033, 41574080, 11774015 and U1530402). This work was performed
199 at HPCAT (Sector 16) and GeoSoilEnviroCARS (The University of Chicago, Sector 13),
200 Advanced Photon Source (APS), Argonne National Laboratory. HPCAT operations are
201 supported by DOE-NNSA's Office of Experimental Sciences. GeoSoilEnviroCARS is supported
202 by the National Science Foundation-Earth Sciences (EAR-1634415) and Department of Energy-
203 GeoSciences (DE-FG02-94ER14466). The Advanced Photon Source is a U.S. Department of
204 Energy (DOE) Office of Science User Facility operated for the DOE Office of Science by
205 Argonne National Laboratory under Contract No. DE-AC02-06CH11357. **Portions of this work**
206 **were performed at the beamline 15U1 of the Shanghai Synchrotron Radiation Facility (SSRF).**

207 **References**

- 208 Barnes, J.D., and Straub, S.M. (2010) Chlorine stable isotope variations in Izu Bonin tephra:
209 Implications for serpentinite subduction. *Chemical Geology*, 272, 62–74.
- 210 Bonifacie, M., Jendrzewski, N., Agrinier, P., Humler, E., Coleman, M., and Javoy, M. (2008)
211 The chlorine isotope composition of earth's mantle. *Science*, 319, 1518–1520.

212 Boulard, E., Guyot, F., Menguy, N., Corgne, A., Auzende, A.L., Perrillat, J.P., and Fiquet, G.
213 CO₂-induced destabilization of pyrite-structured FeO₂H_x in the lower mantle. National
214 Science Review, 5, 870–877.

215 Dorfman, S.M., Meng, Y., Prakapenka, V.B., and Duffy, T.S. (2013) Effects of Fe-enrichment
216 on the equation of state and stability of (Mg,Fe)SiO₃ perovskite. Earth and Planetary
217 Science Letters, 361, 249–257.

218 Du, X., Wang, Z., Wang, Hongbo, Iitaka, T., Pan, Y., Wang, Hui, and Tse, J.S. (2018) Structures
219 and Stability of Iron Halides at the Earth’s Mantle and Core Pressures: Implications for the
220 Missing Halogen Paradox. ACS Earth and Space Chemistry, 2, 711–719.

221 Ford, S.R., Garnero, E.J., and McNamara, A.K. (2006) A strong lateral shear velocity gradient
222 and anisotropy heterogeneity in the lowermost mantle beneath the southern Pacific. Journal
223 of Geophysical Research: Solid Earth, 111, 1–14.

224 Hanyu, T., Shimizu, K., Ushikubo, T., Kimura, J.I., Chang, Q., Hamada, M., Ito, M., Iwamori,
225 H., and Ishikawa, T. (2019) Tiny droplets of ocean island basalts unveil Earth’s deep
226 chlorine cycle. Nature Communications, 10, 4–10.

227 Hiraga, T., Anderson, I.M., and Kohlstedt, D.L. (2004) Grain boundaries as reservoirs of
228 incompatible elements in the Earth’s mantle. Nature, 427, 699–703.

229 Hirose, K., Takafuji, N., Sata, N., and Ohishi, Y. (2005) Phase transition and density of
230 subducted MORB crust in the lower mantle. Earth and Planetary Science Letters, 237, 239–
231 251.

232 Hu, Q., Kim, D.Y., Yang, W., Yang, L., Meng, Y., Zhang, L., and Mao, H.-K. (2016) FeO₂ and
233 FeOOH under deep lower-mantle conditions and Earth's oxygen–hydrogen cycles. *Nature*,
234 534, 241–244.

235 John, T., Scambelluri, M., Frische, M., Barnes, J.D., and Bach, W. (2011) Dehydration of
236 subducting serpentinite: Implications for halogen mobility in subduction zones and the deep
237 halogen cycle. *Earth and Planetary Science Letters*, 308, 65–76.

238 Kendrick, M.A., Hémond, C., Kamenetsky, V.S., Danyushevsky, L., Devey, C.W., Rodemann,
239 T., Jackson, M.G., and Perfit, M.R. (2017) Seawater cycled throughout Earth's mantle in
240 partially serpentinitized lithosphere. *Nature Geoscience*, 10, 222–228.

241 Koemets, E., Yuan, L., Bykova, E., Glazyrin, K., Ohtani, E., and Dubrovinsky, L. (2020)
242 Interaction Between FeOOH and NaCl at Extreme Conditions: Synthesis of Novel
243 Na₂FeCl₄OH_x Compound. *Minerals*, 10, 51.

244 Koemets, E., Leonov, I., Bykov, M., Bykova, E., Chariton, S., Aprilis, G., Fedotenko, T.,
245 Clément, S., Rouquette, J., Haines, J., and others (2021) Revealing the Complex Nature of
246 Bonding in the Binary High-Pressure Compound FeO₂. *Physical Review Letters*, 126, 1–7.

247 Liu, J., Hu, Q., Young Kim, D., Wu, Z., Wang, W., Xiao, Y., Chow, P., Meng, Y., Prakapenka,
248 V.B., Mao, H.K., and others (2017) Hydrogen-bearing iron peroxide and the origin of
249 ultralow-velocity zones. *Nature*, 551, 494–497.

250 Loubeyre, P., LeToullec, R., Wolanin, E., Hanfland, M., and Hausermann, D. (1999) Modulated
251 phases and proton centring in ice observed by X-ray diffraction up to 170 GPa. *Nature*, 397,
252 503–506.

253 Mao, H., Hu, Q., Yang, L., Liu, J., Kim, D.Y., Meng, Y., Zhang, L., Prakapenka, V.B., Yang,
254 W., and Mao, W.L. (2017) When water meets iron at Earth's core-mantle boundary.
255 National Science Review, 4, 870–878.

256 Meng, Y., Hrubiak, R., Rod, E., Boehler, R., and Shen, G. (2015) New developments in laser-
257 heated diamond anvil cell with in situ synchrotron x-ray diffraction at High Pressure
258 Collaborative Access Team. Review of Scientific Instruments, 86, 072201.

259 Nishi, M., Kuwayama, Y., Tsuchiya, J., and Tsuchiya, T. (2017) The pyrite-Type high-pressure
260 form of FeOOH. Nature, 547, 205–208.

261 Prakapenka, V.B., Kubo, A., Kuznetsov, A., Laskin, A., Shkurikhin, O., Dera, P., Rivers, M.L.,
262 and Sutton, S.R. (2008) Advanced flat top laser heating system for high pressure research at
263 GSECARS: Application to the melting behavior of germanium. High Pressure Research, 28,
264 225–235.

265 Ren, Y., Stutzmann, E., van der Hilst, R.D., and Besse, J. (2007) Understanding seismic
266 heterogeneities in the lower mantle beneath the Americas from seismic tomography and
267 plate tectonic history. Journal of Geophysical Research: Solid Earth, 112, 1–15.

268 Roberge, M., Bureau, H., Bolfan-Casanova, N., Raepsaet, C., Surble, S., Khodja, H., Auzende,
269 A.L., Cordier, P., and Fiquet, G. (2017) Chlorine in wadsleyite and ringwoodite: An
270 experimental study. Earth and Planetary Science Letters, 467, 99–107.

271 Scambelluri, M., and Philippot, P. (2001) Deep fluids in subduction zones. Lithos, 55, 213–227.

272 Scambelluri, M., Piccardo, G., Philippot, P., Robbiano, A., and Negretti, L. (1997) High salinity
273 fluid inclusions formed from recycled seawater in deeply subducted alpine serpentinite.
274 Earth and Planetary Science Letters, 148, 485–499.

275 Sharp, Z.D., Shearer, C.K., McKeegan, K.D., Barnes, J.D., and Wang, Y.Q. (2010) The Chlorine
276 Isotope Composition of the Moon and Implications for an Anhydrous Mantle. *Science*, 329,
277 1050–1053.

278 Tschauner, O., Huang, S., Greenberg, E., Prakapenka, V.B., Ma, C., Rossman, G.R., Shen, A.H.,
279 Zhang, D., Newville, M., Lanzirrotti, A., and others (2018) Ice-VII inclusions in diamonds:
280 Evidence for aqueous fluid in Earth’s deep mantle. *Science*, 359, 1136–1139.

281 Yoshino, T., and Jaseem, V. (2018) Fluorine solubility in bridgmanite : A potential fluorine
282 reservoir in the Earth ’ s mantle. *Earth and Planetary Science Letters*, 504, 106–114.

283 Yuan, H., Zhang, L., Ohtani, E., Meng, Y., Greenberg, E., and Prakapenka, V.B. (2019) Stability
284 of Fe-bearing hydrous phases and element partitioning in the system MgO–Al₂O₃–Fe₂O₃–
285 SiO₂–H₂O in Earth’s lowermost mantle. *Earth and Planetary Science Letters*, 524, 115714.

286 Yuan, L., Ohtani, E., Ikuta, D., Kamada, S., Tsuchiya, J., Naohisa, H., Ohishi, Y., and Suzuki, A.
287 (2018) Chemical Reactions Between Fe and H₂O up to Megabar Pressures and Implications
288 for Water Storage in the Earth’s Mantle and Core. *Geophysical Research Letters*, 45, 1330–
289 1338.

290 Zhang, L., Yuan, H., Meng, Y., and Mao, H. (2019) Development of High-Pressure Multigrain
291 X-Ray Diffraction for Exploring the Earth’s Interior. *Engineering*, 5, 441–447.

292

293 **Figure Captions**

294 **Figure 1.** Experimental evidence for (a) CHS06: $\text{Mg}_{0.6}\text{Fe}_{0.4}\text{SiO}_3\text{-H}_2\text{O-NaCl}$ and (b) CSb003:
295 $\text{Mg}_{0.6}\text{Fe}_{0.4}\text{SiO}_3\text{-H}_2\text{O}$. (a) Coexistence of pPv and a previously unknown cubic phase (marked by
296 “C”) at 108(2) GPa after T quench from 1950 K: pPv, $a=2.482(3)$ Å, $b=8.217(14)$ Å, $c=6.177(2)$
297 Å; C, $a=4.9490(2)$ Å. (b) Coexistence of pPv and py- FeO_2H phase at 115(2) GPa after T quench
298 from 2150 K: pPv, $a=2.484(2)$ Å, $b=8.155(12)$ Å, $c=6.171(5)$ Å; py, $a=4.3676(2)$ Å. The
299 calculated peak positions are indicated by ticks. Portions of corresponding spotty XRD patterns
300 of the runs are shown in (c) CHS06 and (d) CSb003, respectively. Experiments were performed
301 with a X-ray wavelength of 0.3344 Å at 13-IDD, APS.

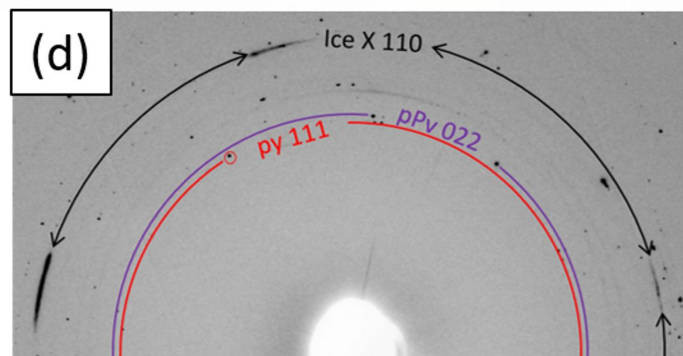
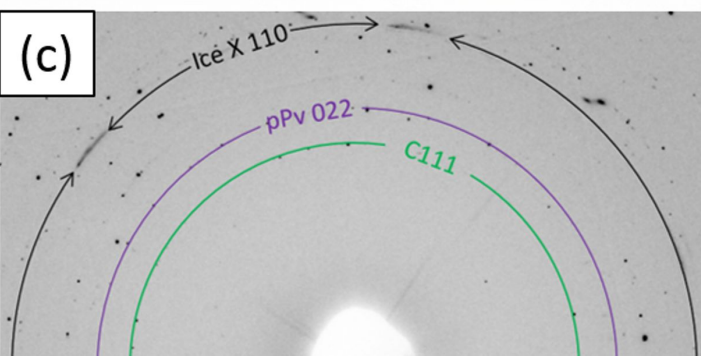
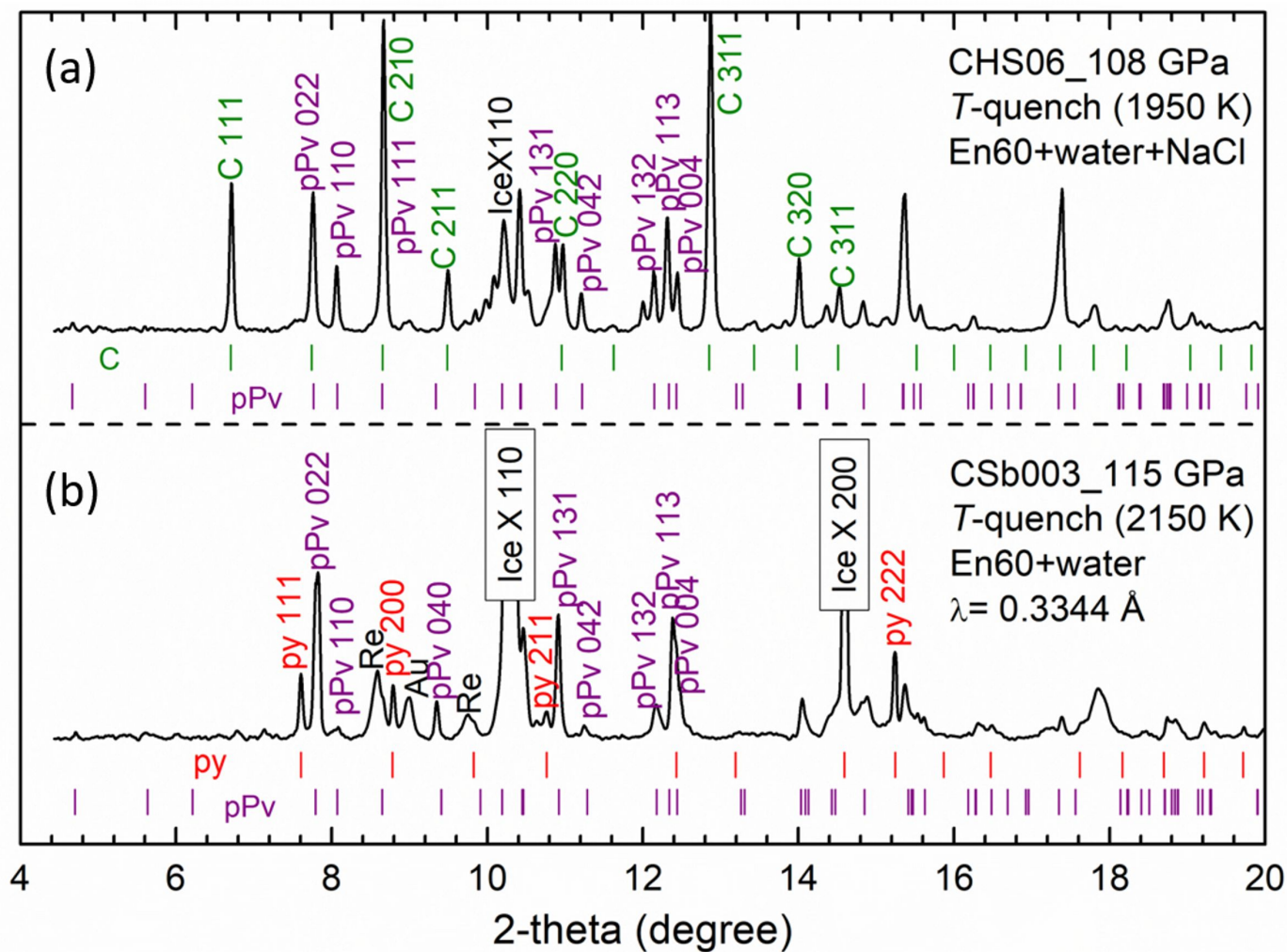
302 **Figure 2.** Experimental evidence for chemical reaction between $\alpha\text{-FeO}_2\text{H}$ and NaCl under high
303 P - T conditions. (a) XRD patterns obtained around 100 GPa at 1700 K (formation of py-phase)
304 and at 2000 K (formation of the “C” phase together with ice X). XRD patterns for (b) Run ETR3
305 at 100(2) GPa and (c) Run CSa010 at 96(2) GPa after T quench. The peak positions of the two
306 orthorhombic phases, the $\text{Na}_2\text{FeCl}_4\text{OH}_x$ phase (space group: $Pbam$) (marked by “N”) with $a =$
307 $8.725(2)$ Å, $b = 6.180(3)$ Å, $c = 3.0679(12)$ Å and the oI phase (space group: $Imm2$) with $a =$
308 $2.5467(5)$ Å, $b = 9.640(2)$ Å, $c = 11.580(2)$ Å at 107(2) GPa from the study by Koemets et al.
309 (2020) are indicated with magenta and orange ticks, respectively, in panel c. Experiments were
310 performed with X-ray wavelengths of 0.4066 and 0.3445 Å for Runs ETR3 and CSa010,
311 respectively, at 16-IDB, APS. The X-axis was set as Q values ($Q = \frac{4\pi\sin\theta}{\lambda}$), where θ and λ
312 represent the diffraction angle and X-ray wavelength, respectively.

313 **Figure 3.** Computational results of the high-pressure PbF_2 -type FeCl_2 phase. (a) Convex hull
314 results of various Fe-Cl at 100 GPa. (b) electronic structure dispersion relations of FeCl_2 at 100

315 GPa with a Fermi level set to 0 (blue dashed line). Harmonic phonon dispersion of FeCl₂ at (c)
316 30 GPa and (d) 100 GPa.

1

Intensity (arb. units)



2

Intensity (arb. units)

